Complete Small-Signal Model of Three-Phase Photovoltaic Inverter Considering the Source and Load Effects

Complete Small-Signal Model of Three-Phase Photovoltaic Inverter Considering the Source and Load Effects

Roosa-Maria Sallinen, Aapo Aapro, Matias Berg, Tuomas Messo
Laboratory of Electrical Energy Engineering,
Tampere University of Technology, Tampere, Finland
Email: roosa-maria.sallinen@tut.fi, aapo.aapro@gmail.com, matias.berg@tut.fi, tuomas.messo@tut.fi

***Abstract*—The amount of photovoltaic inverters connected to the electrical grid is increasing. In order to control the power fed to the grid, the inverter must be controlled, and many different approaches for small-signal modeling have been proposed to facilitate the controller design. However, a solar panel cannot be modeled by an ideal current source and the photovoltaic inverter is not connected to an ideal grid on the load side. This paper proposes a generalized method to include the load and source effects to the dynamic model of a photovoltaic inverter. The method can be used to include the source impedance of the photovoltaic generator and impedance of the distribution line in the small-signal model of the photovoltaic inverter.**

I. Introduction

Renewable energy is revolutionizing the energy production by becoming more and more competitive in terms of price and small environmental effect [1], [2]. Accordingly, the amount of grid-connected inverters is increasing to ramp-up the share of renewable energy in the power system. Three-phase inverters are commonly selected for the power conversion due to their good and well-known performance [3], [4].

However, as a result, the power generation becomes more and more scattered due to the distributed nature of the renewable energy production, and the grid is constructed by various subsystems exhibiting different impedance characteristics depending on the topology of the grid [5]. Generally, a grid with high impedance is considered a weak grid if its short circuit ratio (SCR) is smaller than 10 [6]. This finite grid impedance may cause stability issues in photovoltaic (PV) power plants, such as, harmonic resonances and instability [7]. In order to analyze these phenomena, accurate mathematical models are necessary, which capture the internal dynamic behavior of the converters.

Small-signal modeling is widely utilized to perform reliable and deterministic control design of three-phase power inverters [8]–[12]. Moreover, recent interest toward impedance-based stability analysis has encouraged research on the output impedance characteristics and impedance shaping [5], [13]–[17]. Generally, non-ideal sources and loads affect the formulation of small-signal models by changing the internal behavior (e.g., control performance) of the inverter profoundly [18]. Analysis on the effect of source and load subsystems is always required when connecting the converter power stage to a non-ideal source or load. Practically, this is always the case and, therefore, the inverter cannot be analyzed separately from the source or load dynamics.

Although literature exists around the topic of small-signal modeling with PV and weak grid, the literature partly lacks the full-order or accurate representation of the system dynamics with both source and load subsystems. For example, small-signal modeling of grid-connected PV system was presented in [10], which characterized only the control dynamics of the converter. Similar small-signal analysis was performed in [19], [20], which both lacked the recognition of the effect of a PV generator (PVG) on the system dynamics. Also, no transfer functions in the frequency domain were presented in the paper in [19]. Small-signal analysis was also performed in [8] and [21], yet system transfer functions were not presented and only the time-domain behavior was analyzed. Reduced-order model with load-effect is presented in [18], where all the cross-couplings and dynamics related to q-components are neglected. Thus, the model gives over-simplified and inaccurate results, when the inverter does not operate at unity power factor or the effect of cross-couplings is significant. In [22], the full-order dynamical assessment of all system dynamics were not presented as it concentrated on the proper stability evaluation of the output interface, i.e., only the impedances were analyzed. Thus, the assessment of the load impedance e.g. on the control design was not presented.

Considering the aforementioned factors, this paper presents the full-order small-signal model which can be used to assess the effect of an arbitrary non-ideal current-type source (e.g. PV generator or PV generator with a boost converter) as well as a voltage-type load (e.g. utility grid or grid-forming inverter) on the inverter dynamics in the dq-domain. The model is developed with the multiple-input-multiple-output modeling technique lacked e.g. in [10], [18], [19], [23], which simplifies significantly the derivation of the closed-loop model and improves accuracy of the model [9]. The main contribution of this paper is the full-order small-signal model which considers both the load and source effects. Furthermore, the accuracy of the model is verified from a switching model as well as HIL simulations.

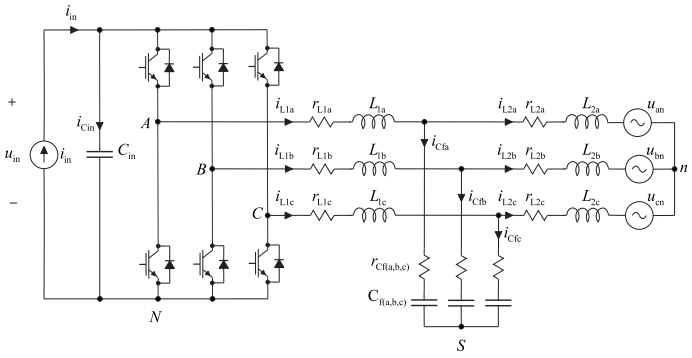

Fig. 1. Power stage of a three-phase grid-connected PV inverter.

II. Small-Signal Modeling

The power stage of a typical grid connected photovoltaic inverter is shown in Fig. 1. By performing averaging and linearization according to technique developed by Middlebrook [24], the linearized state space can be given as in (4). Note that the state matrices **A**, **B**, **C**, and **D** are given in Appendix A. The state variable, input variable, and output variable vectors are defined as (1), (2), and (3), respectively.

$$\begin{aligned}\mathbf{X}(s) &= \left[\hat{i}_{\mathrm{L1d}}, \hat{i}_{\mathrm{L1q}}, \hat{i}_{\mathrm{L2d}}, \hat{i}_{\mathrm{L2q}}, \hat{u}_{\mathrm{Cd}}, \hat{u}_{\mathrm{Cq}}, \hat{u}_{\mathrm{Cin}}\right]^{\mathrm{T}} \\ &= \left[\underline{\hat{i}}_{\mathrm{L1}}, \underline{\hat{i}}_{\mathrm{L2}}, \underline{\hat{u}}_{\mathrm{C}}, \hat{u}_{\mathrm{Cin}}\right]^{\mathrm{T}} \end{aligned} \tag{1}$$

$$\mathbf{U}(s) = \left[\hat{i}_{\mathrm{in}}, \hat{u}_{\mathrm{od}}, \hat{u}_{\mathrm{oq}}, \hat{d}_{\mathrm{d}}, \hat{d}_{\mathrm{q}}\right]^{\mathrm{T}} = \left[\hat{i}_{\mathrm{in}}, \underline{\hat{u}}_{\mathrm{o}}, \underline{\hat{d}}\right]^{\mathrm{T}} \tag{2}$$

$$\mathbf{Y}(s) = \left[\hat{u}_{\mathrm{in}}, \hat{i}_{\mathrm{L1d}}, \hat{i}_{\mathrm{L1q}}, \hat{i}_{\mathrm{L2d}}, \hat{i}_{\mathrm{L2q}}\right]^{\mathrm{T}} = \left[\hat{u}_{\mathrm{in}}, \underline{\hat{i}}_{\mathrm{L1}}, \underline{\hat{i}}_{\mathrm{L2}}\right]^{\mathrm{T}} \tag{3}$$

$$\begin{aligned} s\mathbf{X}(s) &= \mathbf{A}\mathbf{X}(s) + \mathbf{B}\mathbf{U}(s) \\ \mathbf{Y}(s) &= \mathbf{C}\mathbf{X}(s) + \mathbf{D}\mathbf{U}(s). \end{aligned} \tag{4}$$

With minor algebraic manipulation, the equation above can be rearranged and solved with respect to the input and output variables as in (5) and (6).

$$\mathbf{Y}(s) = \left[\mathbf{C}(s\mathbf{I} - \mathbf{A})^{-1}\mathbf{B} + \mathbf{D}\right]\mathbf{U}(s) = \mathbf{G}_{\mathrm{H}}\mathbf{U}(s) \tag{5}$$

$$\mathbf{G}_{\mathrm{H}} = \begin{bmatrix} Z_{\mathrm{in}} & \mathbf{T}_{\mathrm{oi}} & \mathbf{G}_{\mathrm{ci}} \\ \mathbf{G}_{\mathrm{ioL}} & \mathbf{G}_{\mathrm{oL}} & \mathbf{G}_{\mathrm{cL}} \\ \mathbf{G}_{\mathrm{io}} & -\mathbf{Y}_{\mathrm{o}} & \mathbf{G}_{\mathrm{co}} \end{bmatrix} \tag{6}$$

Hence, by selecting the inverter-side inductor current $\underline{\hat{i}}_{\mathrm{L1}}$ as the controlled output current, the control-block diagram of the system can be given as in Fig. 2. Considering the cascaded control structure required by PV applications [23], the DC-link voltage $\underline{\hat{u}}_{\mathrm{o}}$ is treated as another controlled variable. Matrices $\mathbf{G}_{\mathrm{vc}}$ and $\mathbf{G}_{\mathrm{cc}}$ depict the voltage and current controllers, respectively, $\mathbf{G}_{\mathrm{del}}$ represents the system delays, $\mathbf{G}_{\mathrm{se}}$ the voltage sensing gains, and matrix $\mathbf{G}_{\mathrm{PLL}}$ contains the PLL transfer functions which are defined in Appendix B. Matrices $\mathbf{D}$ and $\mathbf{I}_{\mathrm{L1}}$ are gains for the steady state duty-ratio and inductor current.

According to the control-block diagrams and the transfer function matrix in (6), the complete closed-loop dynamics

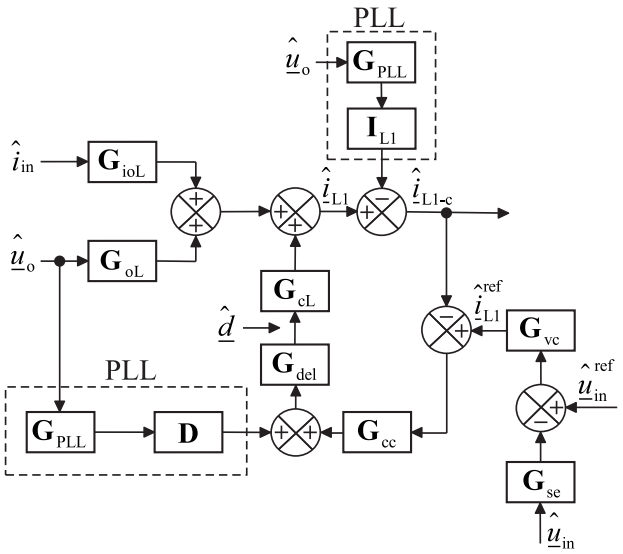

Fig. 2. Closed-loop control block diagram of a three-phase grid-connected VSI-based inverter.

for the converter can be given as in (7)-(15), where $\mathbf{L}_{\mathrm{in}} = \mathbf{G}_{\mathrm{ci}}^{\mathrm{out}}\mathbf{G}_{\mathrm{vc}}$ depicts the DC-link voltage control loop gain. Note that the transfer functions with the superscript 'out' denote that only the current control loops (i.e. the inner control loops of the cascaded control scheme) are connected, and they can be found in Appendix B. In the equations below, Eqs. (7)-(9) represent the input-voltage dynamics, Eqs. (10)-(12) are the inverter-side current dynamics, and (13)-(15) are the grid-current dynamics.

$$Z_{\mathrm{in}}^{\mathrm{tot}} = (\mathbf{I} + \mathbf{L}_{\mathrm{in}})^{-1} Z_{\mathrm{in}}^{\mathrm{out}} \tag{7}$$

$$\mathbf{T}_{\mathrm{oi}}^{\mathrm{tot}} = (\mathbf{I} + \mathbf{L}_{\mathrm{in}})^{-1} \mathbf{T}_{\mathrm{oi}}^{\mathrm{out}} \tag{8}$$

$$\mathbf{G}_{\mathrm{ci}}^{\mathrm{tot}} = (\mathbf{I} + \mathbf{L}_{\mathrm{in}})^{-1} \mathbf{L}_{\mathrm{in}} \tag{9}$$

$$\mathbf{G}_{\mathrm{ioL}}^{\mathrm{tot}} = \mathbf{G}_{\mathrm{ioL}}^{\mathrm{out}} - \mathbf{G}_{\mathrm{cL}}^{\mathrm{out}}\mathbf{G}_{\mathrm{vc}}(\mathbf{I} + \mathbf{L}_{\mathrm{in}})^{-1} Z_{\mathrm{in}}^{\mathrm{out}} \tag{10}$$

$$\mathbf{G}_{\mathrm{oL}}^{\mathrm{tot}} = \mathbf{G}_{\mathrm{oL}}^{\mathrm{out}} - \mathbf{G}_{\mathrm{cL}}^{\mathrm{out}}\mathbf{G}_{\mathrm{vc}}(\mathbf{I} + \mathbf{L}_{\mathrm{in}})^{-1} \mathbf{T}_{\mathrm{oi}}^{\mathrm{out}} \tag{11}$$

$$\mathbf{G}_{\mathrm{cL}}^{\mathrm{tot}} = -\mathbf{G}_{\mathrm{cL}}^{\mathrm{out}}\left[\mathbf{G}_{\mathrm{vc}}(\mathbf{I} + \mathbf{L}_{\mathrm{in}})^{-1}\mathbf{L}_{\mathrm{in}} - \mathbf{G}_{\mathrm{vc}}\right] \tag{12}$$

$$\mathbf{G}_{\mathrm{io}}^{\mathrm{tot}} = \mathbf{G}_{\mathrm{io}}^{\mathrm{out}} - \mathbf{G}_{\mathrm{co}}^{\mathrm{out}}\mathbf{G}_{\mathrm{vc}}(\mathbf{I} + \mathbf{L}_{\mathrm{in}})^{-1} Z_{\mathrm{in}}^{\mathrm{out}} \tag{13}$$

$$\mathbf{Y}_{\mathrm{o}}^{\mathrm{tot}} = \mathbf{Y}_{\mathrm{o}}^{\mathrm{out}} + \mathbf{G}_{\mathrm{co}}^{\mathrm{out}}\mathbf{G}_{\mathrm{vc}}(\mathbf{I} + \mathbf{L}_{\mathrm{in}})^{-1} \mathbf{T}_{\mathrm{oi}}^{\mathrm{out}} \tag{14}$$

$$\mathbf{G}_{\mathrm{co}}^{\mathrm{tot}} = -\mathbf{G}_{\mathrm{co}}^{\mathrm{out}}\left[\mathbf{G}_{\mathrm{vc}}(\mathbf{I} + \mathbf{L}_{\mathrm{in}})^{-1}\mathbf{L}_{\mathrm{in}} - \mathbf{G}_{\mathrm{vc}}\right] \tag{15}$$

Above equations determine the closed-loop dynamics of the grid-connected converter with ideal current source and voltage load (i.e., zero impedance). Next sections present the multivariable modeling procedure and analysis of both source- and load-affected small-signal models.

III. Source-affected system dynamics

Photovoltaic generator induces varying dynamical resistance (r_{pv}) connected across the input terminal of the converter. This has to be considered in the dynamical model in order to analyze the converter dynamics correctly [23]. As shown in Fig. 3, a non-ideal source with finite admittance Y_{s} is assumed here, which can be included in the open-loop dynamics of the system. Accordingly, the real input current ($\hat{i}_{\mathrm{in}}$) of the converter is affected by the non-ideal source current $\hat{i}_{\mathrm{inS}}$ as well as the parallel admittance Y_{s} and can be expressed as

$$\hat{i}_{\mathrm{in}} = \hat{i}_{\mathrm{inS}} - Y_{\mathrm{s}}\hat{u}_{\mathrm{in}}. \tag{16}$$

Consequently, the input voltage dynamics can be presented by substituting (16) into the nominal open-loop input voltage dynamics as

$$\hat{u}_{\mathrm{in}} = Z_{\mathrm{in}}\left(\hat{i}_{\mathrm{inS}} - Y_{\mathrm{s}}\hat{u}_{\mathrm{in}}\right) + \mathbf{T}_{\mathrm{oi}}\underline{\hat{u}}_{\mathrm{o}} + \mathbf{G}_{\mathrm{ci}}\underline{\hat{d}}, \tag{17}$$

$$\hat{u}_{\mathrm{in}} = \frac{Z_{\mathrm{in}}}{1+Z_{\mathrm{in}}Y_{\mathrm{s}}}\hat{i}_{\mathrm{inS}} + \frac{\mathbf{T}_{\mathrm{oi}}}{1+Z_{\mathrm{in}}Y_{\mathrm{s}}}\underline{\hat{u}}_{\mathrm{o}} + \frac{\mathbf{G}_{\mathrm{ci}}}{1+Z_{\mathrm{in}}Y_{\mathrm{s}}}\underline{\hat{d}}.$$

The source-affected input current can be expressed as in (18), which is then substituted into the open-loop dynamics of the inverter and grid currents.

$$\hat{i}_{\mathrm{in}} = \left(1 - \frac{Z_{\mathrm{in}}Y_{\mathrm{s}}}{1+Z_{\mathrm{in}}Y_{\mathrm{s}}}\right)\hat{i}_{\mathrm{inS}} - \frac{Y_{\mathrm{s}}\mathbf{T}_{\mathrm{oi}}}{1+Z_{\mathrm{in}}Y_{\mathrm{s}}}\underline{\hat{u}}_{\mathrm{o}} - \frac{Y_{\mathrm{s}}\mathbf{G}_{\mathrm{ci}}}{1+Z_{\mathrm{in}}Y_{\mathrm{s}}}\underline{\hat{d}}. \tag{18}$$

Accordingly, the source-affected dynamics for input voltage, inductor current, and grid current can be given by

$$\hat{u}_{\mathrm{in}} = \frac{Z_{\mathrm{in}}}{1+Z_{\mathrm{in}}Y_{\mathrm{s}}}\hat{i}_{\mathrm{inS}} + \frac{\mathbf{T}_{\mathrm{oi}}}{1+Z_{\mathrm{in}}Y_{\mathrm{s}}}\underline{\hat{u}}_{\mathrm{o}} + \frac{\mathbf{G}_{\mathrm{ci}}}{1+Z_{\mathrm{in}}Y_{\mathrm{s}}}\underline{\hat{d}}, \tag{19}$$

$$\begin{aligned}\underline{\hat{i}}_{\mathrm{L1}} = {} & \mathbf{G}_{\mathrm{ioL}}\left(1 - \frac{Z_{\mathrm{in}}Y_{\mathrm{s}}}{1+Z_{\mathrm{in}}Y_{\mathrm{s}}}\right)\hat{i}_{\mathrm{inS}} \\ & + \left(\mathbf{G}_{\mathrm{oL}} - \mathbf{G}_{\mathrm{ioL}}\frac{Y_{\mathrm{s}}\mathbf{T}_{\mathrm{oi}}}{1+Z_{\mathrm{in}}Y_{\mathrm{s}}}\right)\underline{\hat{u}}_{\mathrm{o}} \\ & + \left(\mathbf{G}_{\mathrm{cL}} - \mathbf{G}_{\mathrm{ioL}}\frac{Y_{\mathrm{s}}\mathbf{G}_{\mathrm{ci}}}{1+Z_{\mathrm{in}}Y_{\mathrm{s}}}\right)\underline{\hat{d}},\end{aligned} \tag{20}$$

$$\begin{aligned}\underline{\hat{i}}_{\mathrm{L2}} = {} & \mathbf{G}_{\mathrm{io}}\left(1 - \frac{Z_{\mathrm{in}}Y_{\mathrm{s}}}{1+Z_{\mathrm{in}}Y_{\mathrm{s}}}\right)\hat{i}_{\mathrm{inS}} \\ & - \left(\mathbf{Y}_{\mathrm{o}} - \mathbf{G}_{\mathrm{io}}\frac{Y_{\mathrm{s}}\mathbf{T}_{\mathrm{oi}}}{1+Z_{\mathrm{in}}Y_{\mathrm{s}}}\right)\underline{\hat{u}}_{\mathrm{o}} \\ & + \left(\mathbf{G}_{\mathrm{co}} - \mathbf{G}_{\mathrm{io}}\frac{Y_{\mathrm{s}}\mathbf{G}_{\mathrm{ci}}}{1+Z_{\mathrm{in}}Y_{\mathrm{s}}}\right)\underline{\hat{d}}.\end{aligned} \tag{21}$$

IV. Load-affected system dynamics

By considering the output terminal of the converter as the Point of Common Coupling (PCC), the grid-feeding converter observes a series input impedance with the ideal grid voltage. This grid impedance affects the voltage at the PCC by causing phase and magnitude deviation compared to the ideal grid which, in turn, affects the dynamics of the converter.

Before analyzing the effect of the load on the system dynamics, the reference frame for the analysis must be selected [22]. The converter reference frame is different than

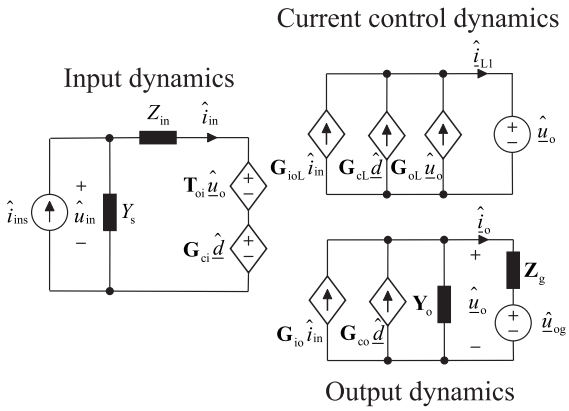

Fig. 3. Load-affected model of a grid-connected inverter at open loop.

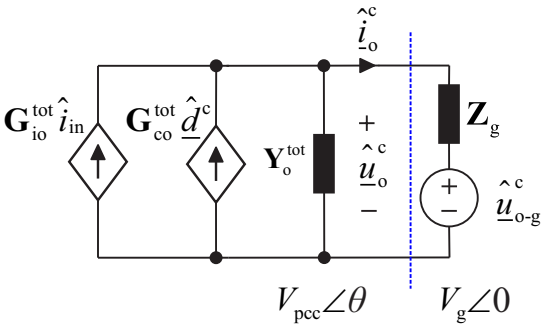

Fig. 4. The converter and grid reference frames.

the grid reference frame, which must be taken into account when deriving the model. By overlooking the aforementioned factor, the model would yield inaccurate predictions, especially considering the cross-coupling elements between the d and q-components. The effect of the load can be derived into the closed-loop dynamics by first analyzing the interface at the PCC according to Fig. 4.

In Fig. 4, the superscript 'c' in the variables denotes that the corresponding variable is inside the converter reference frame. Hereinafter, the superscript 'g' denotes that a variable is in the grid reference frame. The relation between the converter and grid reference frames can be given as

$$\underline{x}^{\mathrm{c}} = \mathbf{T}_{\mathrm{dq}}\underline{x}^{\mathrm{g}}, \tag{22}$$

where the transformation matrix $\mathbf{T}_{\mathrm{dq}}$ can be expressed as

$$\mathbf{T}_{\mathrm{dq}} = \begin{bmatrix} \cos\theta & \sin\theta \\ -\sin\theta & \cos\theta \end{bmatrix}. \tag{23}$$

The angle difference θ between the reference frames can be calculated e.g. from the steady-state values of the grid currents and grid voltages if the grid impedance is known. Alternatively, the steady-state angle difference can be obtained by simulations.

By acknowledging the aforementioned reference-frame factor, the load-affected model can be developed by first solving

the grid current under weak grid. From Fig. 4, the PCC voltage can be given as

$$\hat{\underline{u}}_{\mathrm{o}}^{\mathrm{c}} = \hat{\underline{u}}_{\mathrm{o\text{-}g}}^{\mathrm{c}} + \mathbf{Z}_{\mathrm{g}}\hat{\underline{i}}_{\mathrm{o}}^{\mathrm{c}}, \tag{24}$$

where the grid-impedance matrix is generally presented as

$$\mathbf{Z}_{\mathrm{g}} = \begin{bmatrix} Z_{\mathrm{g\text{-}d}} & Z_{\mathrm{g\text{-}qd}} \\ Z_{\mathrm{g\text{-}dq}} & Z_{\mathrm{g\text{-}q}} \end{bmatrix}. \tag{25}$$

From the closed-loop dynamics, the grid current $\hat{\underline{i}}_{\mathrm{o}}^{\mathrm{c}}$ can be further expressed as in (26). Note that the superscript 'tot' is omitted from the following equations for simplicity.

$$\hat{\underline{u}}_{\mathrm{o}}^{\mathrm{c}} = \hat{\underline{u}}_{\mathrm{o\text{-}g}}^{\mathrm{c}} + \mathbf{Z}_{\mathrm{g}}\left(\mathbf{G}_{\mathrm{io}}\hat{\underline{i}}_{\mathrm{in}} - \mathbf{Y}_{\mathrm{o}}\hat{\underline{u}}_{\mathrm{o}}^{\mathrm{c}} + \mathbf{G}_{\mathrm{co}}\hat{\underline{d}}^{\mathrm{c}}\right) \tag{26}$$

Solving the non-ideal PCC voltage from (26) yields

$$\begin{aligned}\hat{\underline{u}}_{\mathrm{o}}^{\mathrm{c}} = {} & (\mathbf{I}+\mathbf{Z}_{\mathrm{g}}\mathbf{Y}_{\mathrm{o}})^{-1}\mathbf{Z}_{\mathrm{g}}\mathbf{G}_{\mathrm{io}}\hat{\underline{i}}_{\mathrm{in}} + (\mathbf{I}+\mathbf{Z}_{\mathrm{g}}\mathbf{Y}_{\mathrm{o}})^{-1}\hat{\underline{u}}_{\mathrm{o\text{-}g}}^{\mathrm{c}} \\ & +(\mathbf{I}+\mathbf{Z}_{\mathrm{g}}\mathbf{Y}_{\mathrm{o}})^{-1}\mathbf{Z}_{\mathrm{g}}\mathbf{G}_{\mathrm{co}}\hat{\underline{d}}^{\mathrm{c}},\end{aligned} \tag{27}$$

which can be substituted into the non-ideal PCC voltage denoted by $\hat{\underline{u}}_{\mathrm{o}}$. Thus, the load-affected closed-loop model, i.e. the equations for DC-link voltage, inverter-side current, and the grid current, can given by (28), (29), and (30), respectively.

$$\begin{aligned}\hat{u}_{\mathrm{in}} = {} & \left(Z_{\mathrm{in}} + \mathbf{T}_{\mathrm{oi}}(\mathbf{I}+\mathbf{Z}_{\mathrm{g}}\mathbf{Y}_{\mathrm{o}})^{-1}\mathbf{Z}_{\mathrm{g}}\mathbf{G}_{\mathrm{io}}\right)\hat{\underline{i}}_{\mathrm{in}} \\ & +\mathbf{T}_{\mathrm{oi}}(\mathbf{I}+\mathbf{Z}_{\mathrm{g}}\mathbf{Y}_{\mathrm{o}})^{-1}\hat{\underline{u}}_{\mathrm{o\text{-}g}}^{\mathrm{c}} \\ & + \left(\mathbf{G}_{\mathrm{ci}} + \mathbf{T}_{\mathrm{oi}}(\mathbf{I}+\mathbf{Z}_{\mathrm{g}}\mathbf{Y}_{\mathrm{o}})^{-1}\mathbf{Z}_{\mathrm{g}}\mathbf{G}_{\mathrm{co}}\right)\hat{\underline{d}}^{\mathrm{c}}\end{aligned} \tag{28}$$

$$\begin{aligned}\hat{\underline{i}}_{\mathrm{L1}}^{\mathrm{c}} = {} & \left(\mathbf{G}_{\mathrm{ioL}} + \mathbf{G}_{\mathrm{oL}}(\mathbf{I}+\mathbf{Z}_{\mathrm{g}}\mathbf{Y}_{\mathrm{o}})^{-1}\mathbf{Z}_{\mathrm{g}}\mathbf{G}_{\mathrm{io}}\right)\hat{\underline{i}}_{\mathrm{in}} \\ & +\mathbf{G}_{\mathrm{oL}}(\mathbf{I}+\mathbf{Z}_{\mathrm{g}}\mathbf{Y}_{\mathrm{o}})^{-1}\hat{\underline{u}}_{\mathrm{o\text{-}g}}^{\mathrm{c}} \\ & + \left(\mathbf{G}_{\mathrm{cL}} + \mathbf{G}_{\mathrm{oL}}(\mathbf{I}+\mathbf{Z}_{\mathrm{g}}\mathbf{Y}_{\mathrm{o}})^{-1}\mathbf{Z}_{\mathrm{g}}\mathbf{G}_{\mathrm{co}}\right)\hat{\underline{d}}^{\mathrm{c}}\end{aligned} \tag{29}$$

$$\begin{aligned}\hat{\underline{i}}_{\mathrm{o}}^{\mathrm{c}} = {} & \left(\mathbf{G}_{\mathrm{io}} - \mathbf{Y}_{\mathrm{o}}(\mathbf{I}+\mathbf{Z}_{\mathrm{g}}\mathbf{Y}_{\mathrm{o}})^{-1}\mathbf{Z}_{\mathrm{g}}\mathbf{G}_{\mathrm{io}}\right)\hat{\underline{i}}_{\mathrm{in}} \\ & -\mathbf{Y}_{\mathrm{o}}(\mathbf{I}+\mathbf{Z}_{\mathrm{g}}\mathbf{Y}_{\mathrm{o}})^{-1}\hat{\underline{u}}_{\mathrm{o\text{-}g}}^{\mathrm{c}} \\ & + \left(\mathbf{G}_{\mathrm{co}} - \mathbf{Y}_{\mathrm{o}}(\mathbf{I}+\mathbf{Z}_{\mathrm{g}}\mathbf{Y}_{\mathrm{o}})^{-1}\mathbf{Z}_{\mathrm{g}}\mathbf{G}_{\mathrm{co}}\right)\hat{\underline{d}}^{\mathrm{c}}\end{aligned} \tag{30}$$

Regarding the stability analysis of the grid interface, the generalized Nyquist stability criterion is required for the assessment. However, the above equations are presented for the inverter reference frame which does not suffice when analyzing the system from the grid point-of-view. The grid current and the grid voltage in the converter reference frame must be represented in the real grid reference frame. Accordingly, the coordinate transformation can be performed by denoting

$$\hat{\underline{i}}_{\mathrm{o}}^{\mathrm{c}} = \mathbf{T}_{\mathrm{dq}}\hat{\underline{i}}_{\mathrm{o}}^{\mathrm{g}} \rightarrow \hat{\underline{i}}_{\mathrm{o}}^{\mathrm{g}} = \mathbf{T}_{\mathrm{dq}}{}^{-1}\hat{\underline{i}}_{\mathrm{o}}^{\mathrm{c}}, \quad \hat{\underline{u}}_{\mathrm{o\text{-}g}}^{\mathrm{c}} = \mathbf{T}_{\mathrm{dq}}\hat{\underline{u}}_{\mathrm{o\text{-}g}}^{\mathrm{g}}. \tag{31}$$

Note that the interpretation of the coordinate transformation should be given careful attention. In particular, it is not feasible to analyze some of the transfer functions in both reference frames, whereas in a practical setup some may not be measurable. However, considering the above, the correct dynamics of the grid-connected inverter are obtained. Note that the model is also valid for the analysis of the open-loop dynamics. Stability assessment can be, therefore, readily applied to verify the stability of the grid interface as well as its effects on the control system performance of the converter. Note that the stability analysis is not the topic of interest in this paper and, therefore, is omitted.

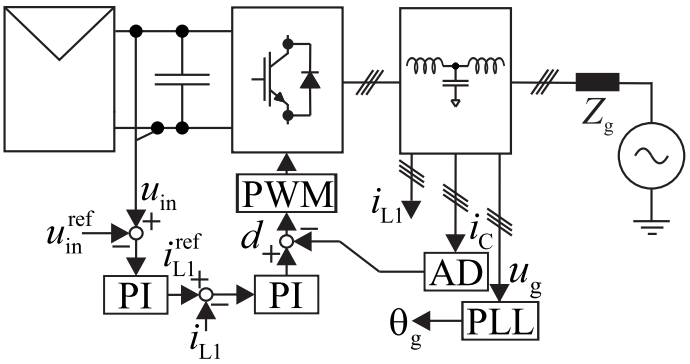

Fig. 5. Depiction of the power stage and control system configuration.

TABLE I
OPERATING POINT AND COMPONENT VALUES.

Parameter	Value	Parameter	Value
U_{in}	750 V	C_{in}	1.9 mF
I_{in}	20 A	L_1	2.5 mH
$U_{\mathrm{grid,rms}}$	230 V	r_{L1}	65 mΩ
$\omega_{\mathrm{grid}}, \omega_{\mathrm{s}}$	$2\pi 60$ rad/s	C_{f}	10 μF
f_{s}	20 kHz	r_{Cf}	10 mΩ
f_{res}	2.29 kHz	L_2	0.6 mH
$f_{\mathrm{s}}/f_{\mathrm{res}}$	8.7	r_{L2}	22 mΩ
r_{sw}	10 mΩ		

V. Model Verification

This section presents the simulation results in order to validate the accuracy of the developed model. The measurements are carried with both Matlab Simulink software and with Typhoon HIL development platform. The frequency-domain data is measured by using PRBS-injection method, which can also be readily applied for experimental inverters [25] as well as by using a commercial frequency response analyzer with sine-sweep.

The overall system configuration with the power stage and the control structures is presented in Fig. 5. It consists of the PV generator, inverter bridge, a grid filter, finite grid impedance with utility grid, and the control structure. A cascaded control system is utilized as is the common practice in PV-inverter systems. Table I presents the power stage and component values used in the simulations. The superscript "tot-LS" is used to highlight that the model includes both the source and the load effects. A delay of 1.5 times the switching period was used.

In order to validate the model, the closed-loop frequency responses of the system transfer functions are presented. This is done by utilizing Matlab Simulink software and PRBS-injection method. Note that in all the following figures, the predicted transfer functions are presented by dotted lines, and solid lines represent the frequency responses identified from a MATLAB switching model. First, the input-voltage related transfer functions are verified and presented in Figs. 6-8. Then, the inverter-side current and grid current transfer functions are presented in Figs. 9 and 10-13, respectively. Based on the

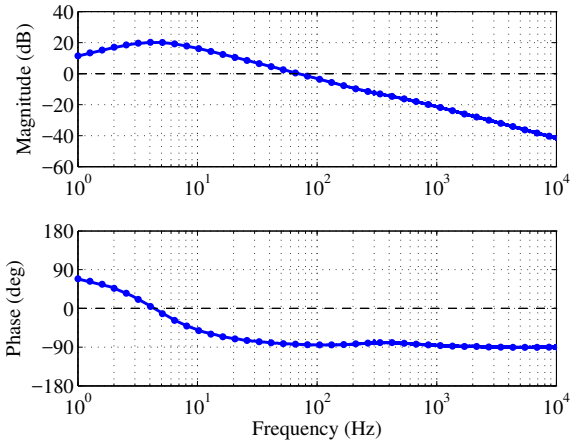

Fig. 6. Simulated (solid line) and modeled (dotted line) input impedance $Z_{\text{in}}^{\text{tot-LS}}$.

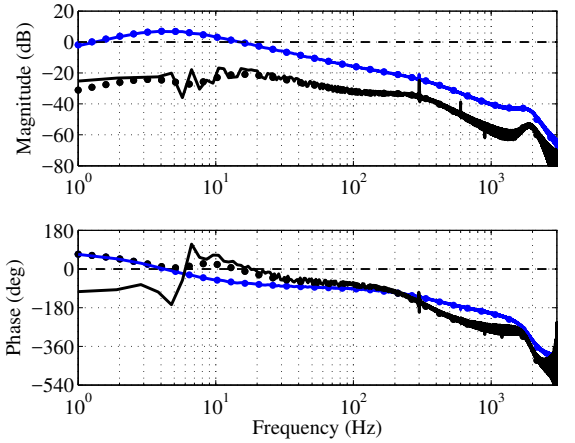

Fig. 7. Simulated (solid line) and modeled (dotted line) d-component (blue) and q-component (black) of transmittance $\mathbf{T}_{\text{oi}}^{\text{tot-LS}}$.

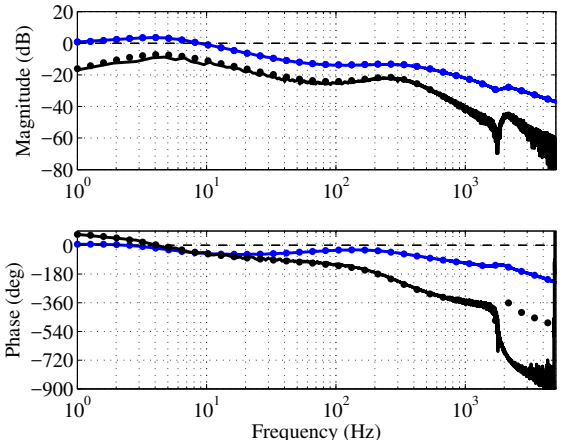

Fig. 8. Simulated (solid line) and modeled (dotted line) d-component (blue) and q-component (black) of control-to-input voltage transfer function $\mathbf{G}_{\text{ci}}^{\text{tot-LS}}$.

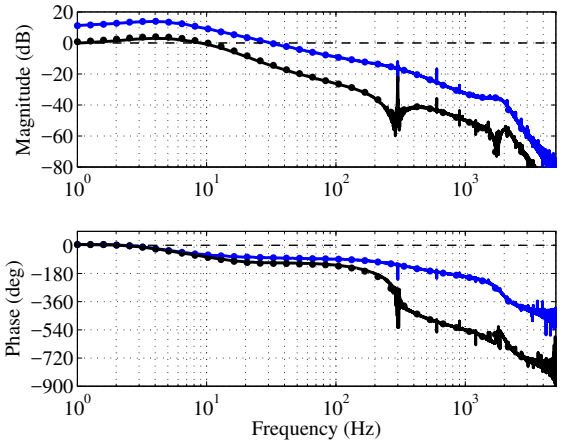

Fig. 9. Simulated (solid line) and modeled (dotted line) d-component (blue) and q-component (black) of input-to-output current transfer function $\mathbf{G}_{\text{ioL}}^{\text{tot-LS}}$.

results, the developed model is shown to be very accurate at predicting the dynamic behavior of the converter with both non-ideal source and load. Good overall accuracy is evident between the predicted and identified frequency responses.

Furthermore, to verify the accuracy of the model at different operating points and to demonstrate the effect the load and the source can have on the system dynamics, the closed-loop frequency responses of relevant transfer functions are compared regarding changes in the source and load conditions. The simulations are performed with Typhoon HIL development platform from which the frequency responses are identified using a separate frequency response analyzer with sine-sweep, except for the Fig. 17, in which Simulink was used.

In Fig. 14, the output-side admittance $\mathbf{Y}_{\text{o}}^{\text{tot-LS}}$ is shown at different PVG operating points, i.e., when the PVG is operating in constant current region (CCR), at the maximum power point (MPP), and in constant voltage region (CVR). The points of interest have been chosen as ± 10 % of the MPP voltage (here 750 V) to represent relatively small variations in the voltage under constant irradiation and temperature (STC). The chosen variations in the MPP voltage imply a reduction in the produced power of 5 % and 10 % in CCR and CVR, respectively. Under real conditions, the variations may be significantly larger depending on the MPP tracker and the irradiance fluctuation etc. The dynamic resistance of the PVG depends highly on its operating point and has an effect on the system dynamics. Accordingly, as can be seen in the figure, the transfer functions are slightly different. However, the model predicts them correctly and with good accuracy.

Fig. 15 shows the d-component of the output-side admittance $\mathbf{Y}_{\text{o}}^{\text{tot-LS}}$ when the grid inductance is decreased from 8 mH to 2 mH. Note that here the admittance is considered from the ideal grid point of view. It is clear that the grid impedance has a strong effect on the output-side admittance at higher frequencies. Adverse interaction with the grid is stronger when the grid conditions are weak, i.e., the grid impedance is high. This affects the output-side admittance by lowering the gain, as can be seen in the figure.

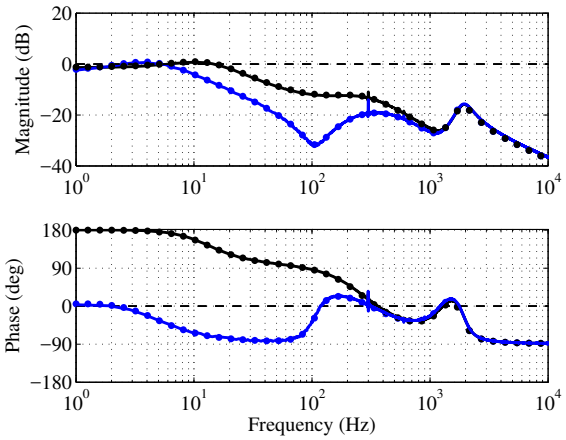

Fig. 10. Simulated (solid line) and modeled (dotted line) d-component (blue) and q-component (black) of output admittance $\mathbf{Y}_{\mathrm{o}}^{\text{tot-LS}}$.

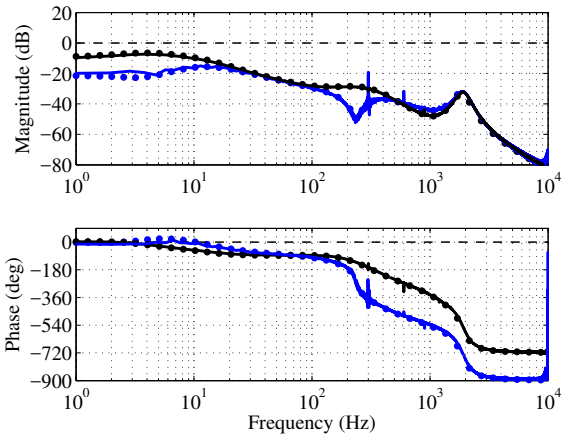

Fig. 11. Simulated (solid line) and modeled (dotted line) qd-component (blue) and dq-component (black) of output admittance $\mathbf{Y}_{\mathrm{o}}^{\text{tot-LS}}$.

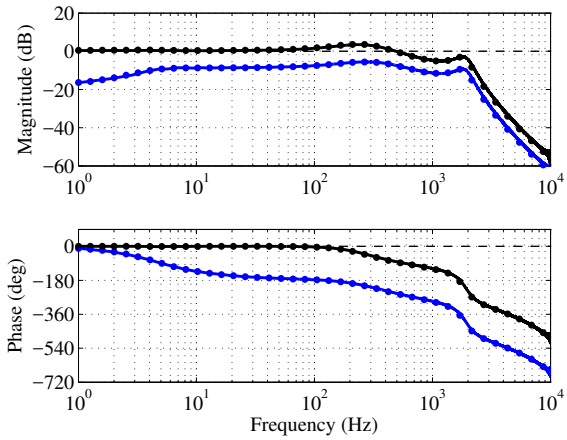

Fig. 12. Simulated (solid line) and modeled (dotted line) d-component (blue) and q-component (black) of control-to-output current transfer function $\mathbf{G}_{\mathrm{co}}^{\text{tot-LS}}$.

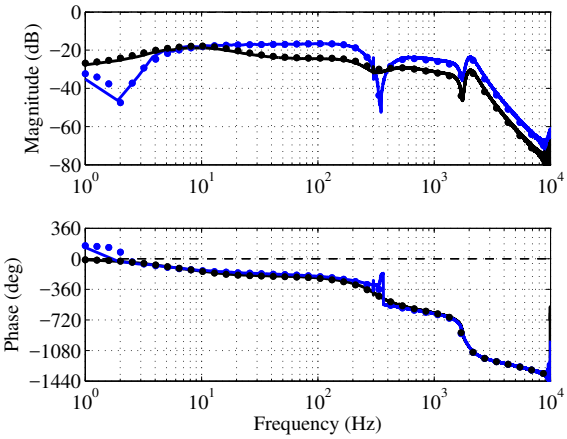

Fig. 13. Simulated (solid line) and modeled (dotted line) qd-component (blue) and dq-component (black) of control-to-output current transfer function $\mathbf{G}_{\mathrm{co}}^{\text{tot-LS}}$.

The qd-component of the output-side admittance $\mathbf{Y}_{\mathrm{o}}^{\text{tot-LS}}$ with and without the load effect is shown in Fig. 16. The difference between the two cases is significant. Thus, in order to guarantee reliable stability analysis, the effect of the load cannot be ignored, i.e., the grid cannot be estimated as ideal three-phase voltage source.

Fig. 17 presents the q-component of the control-to-output current transfer function $\mathbf{G}_{\mathrm{cL}}^{\text{tot-LS}}$ when the grid inductance is decreased from 8 mH to 2 mH. Based on the figure, the reduction in the grid inductance improves the bandwidth of the current control. The effect of the grid impedance on the control-to-output current transfer function should be taken into account especially when designing reactive power or droop control. The frequency response also reveals that the inverter may amplify noise in the kilohertz-range due to magnitude close to unity.

The figures show a good correspondence between the predicted and identified frequency responses. As a result, the model allows the effects of both the source and the load to be taken into account. Thus, the model can be used to perform reliable and deterministic control design and stability validation under varying operating conditions.

VI. Conclusion

The main contribution of this paper is the full-order small-signal model of a grid-connected PV inverter in the dq-domain which considers both the load and source effects. The model can be used to assess the effect of an arbitrary non-ideal current-type source (e.g. PV generator or PV generator with a boost converter) as well as a voltage-type load (e.g. utility grid or grid-forming inverter) on the inverter dynamics. Thus, the full dynamic analysis can be performed as e.g. the control and impedance dynamics are accurately predicted. The model is developed with the multiple-input-multiple-output modeling technique which simplifies significantly the derivation of the closed-loop model and improves the accuracy of the model [9]. Furthermore, the accuracy of the model is verified from a switching model as well as using HIL simulations.

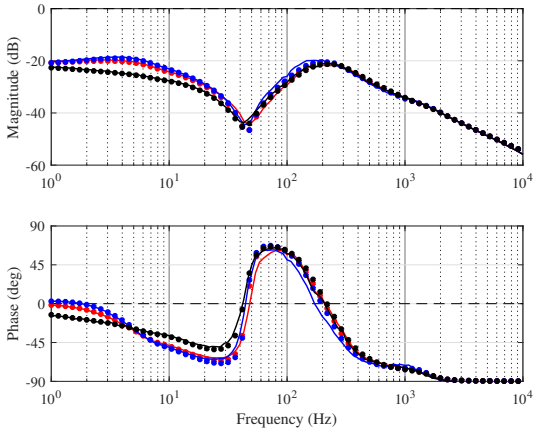

Fig. 14. HIL-simulation result (solid line) and modeled (dotted line) d-components of the output-side admittance $\mathbf{Y}_{\mathrm{o}}^{\text{tot-LS}}$ at different PVG operating points: MPP (red), CCR (blue), and CVR (black).

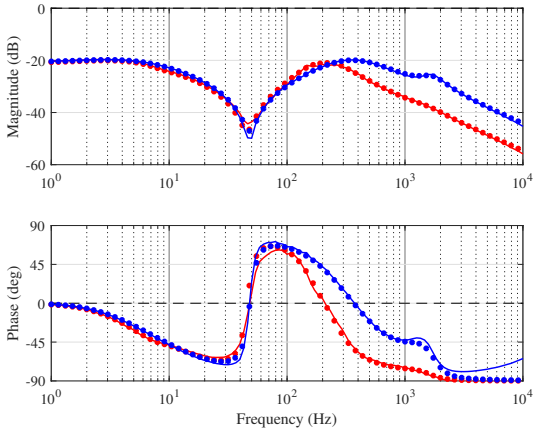

Fig. 15. HIL-simulation result (solid line) and modeled (dotted line) d-component of the output-side admittance $\mathbf{Y}_{\mathrm{o}}^{\text{tot-LS}}$ when the grid inductance is decreased from 8 mH (red) to 2 mH (blue).

APPENDIX A

The system state matrices presented in Section II in (4) are given as follows. In **A**-**D**, r_{eq} is the combined inverter-side inductor ESR and the switch on-time resistance, r_{C} is the LCL-filter capacitor ESR, r_{L2} is the grid-inductor ESR, C_{in} is the input filter capacitor, L_1 is the inverter-side inductance, L_2 is the grid-side inductance, C_{f} is the LCL-filter capacitance, U_{in} is the steady-state inverter input voltage, I_{in} is the steady-state inverter input current, D_{d} is the d-component of the steady-state duty ratio, D_{q} is the q-component of the steady-state duty ratio, and ω_{s} is the grid fundamental frequency.

$$\mathbf{A} = \begin{bmatrix} -\frac{r_{\mathrm{eq}}}{L_1} & \omega_{\mathrm{s}} & \frac{r_{\mathrm{C}}}{L_1} & 0 & -\frac{1}{L_1} & 0 & \frac{D_{\mathrm{d}}}{L_1} \\ -\omega_{\mathrm{s}} & -\frac{r_{\mathrm{eq}}}{L_1} & 0 & \frac{r_{\mathrm{C}}}{L_1} & 0 & -\frac{1}{L_1} & \frac{D_{\mathrm{q}}}{L_1} \\ \frac{r_{\mathrm{C}}}{L_2} & 0 & -\frac{r_{\mathrm{L2}}+r_{\mathrm{C}}}{L_2} & \omega_{\mathrm{s}} & \frac{1}{L_2} & 0 & 0 \\ 0 & \frac{r_{\mathrm{C}}}{L_2} & -\omega_{\mathrm{s}} & -\frac{r_{\mathrm{L2}}+r_{\mathrm{C}}}{L_2} & 0 & \frac{1}{L_2} & 0 \\ \frac{1}{C_{\mathrm{f}}} & 0 & -\frac{1}{C_{\mathrm{f}}} & 0 & 0 & \omega_{\mathrm{s}} & 0 \\ 0 & \frac{1}{C_{\mathrm{f}}} & 0 & -\frac{1}{C_{\mathrm{f}}} & -\omega_{\mathrm{s}} & 0 & 0 \\ -\frac{3}{2}\frac{D_{\mathrm{d}}}{C_{\mathrm{in}}} & -\frac{3}{2}\frac{D_{\mathrm{q}}}{C_{\mathrm{in}}} & 0 & 0 & 0 & 0 & 0 \end{bmatrix} \tag{32}$$

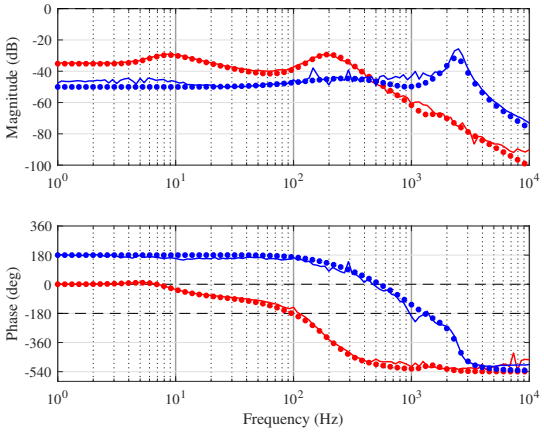

Fig. 16. HIL-simulation result (solid line) and modeled (dotted line) qd-component of the output-side admittance $\mathbf{Y}_{\mathrm{o}}^{\text{tot-LS}}$ with (red) and without (blue) the load effect.

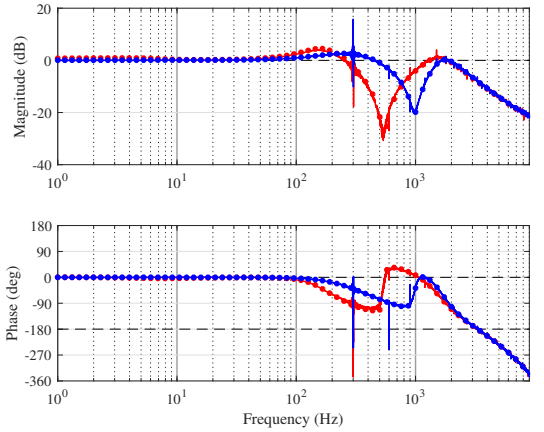

Fig. 17. Simulated (solid line) and modeled (dotted line) q-component of the control-to-output current transfer function $\mathbf{G}_{\mathrm{cL}}^{\text{tot-LS}}$ when the grid inductance is decreased from 8 mH (red) to 2 mH (blue).

$$\mathbf{B} = \begin{bmatrix} 0 & 0 & 0 & \frac{U_{\mathrm{in}}}{L_1} & 0 \\ 0 & 0 & 0 & 0 & \frac{U_{\mathrm{in}}}{L_1} \\ 0 & -\frac{1}{L_2} & 0 & 0 & 0 \\ 0 & 0 & -\frac{1}{L_2} & 0 & 0 \\ 0 & 0 & 0 & 0 & 0 \\ 0 & 0 & 0 & 0 & 0 \\ \frac{1}{C_{\mathrm{in}}} & 0 & 0 & -\frac{I_{\mathrm{in}}}{D_{\mathrm{d}}C_{\mathrm{in}}} & 0 \end{bmatrix} \tag{33}$$

$$\mathbf{C} = \begin{bmatrix} 0 & 0 & 0 & 0 & 0 & 0 & 1 \\ 1 & 0 & 0 & 0 & 0 & 0 & 0 \\ 0 & 1 & 0 & 0 & 0 & 0 & 0 \\ 0 & 0 & 1 & 0 & 0 & 0 & 0 \\ 0 & 0 & 0 & 1 & 0 & 0 & 0 \end{bmatrix} \tag{34}$$

$$\mathbf{D} = \mathbf{0} \tag{35}$$

APPENDIX B

The closed-loop transfer function matrices presented in Section II in (7)-(15) can be derived from the input and output dynamics in (5) and (6) and Fig. 2 by ignoring the input-voltage control loop and can be given as follows:

$$\mathbf{T}_{\mathrm{oi}}^{\mathrm{out}} = \mathbf{T}_{\mathrm{oi}} - \mathbf{G}_{\mathrm{ci}}\mathbf{G}_{\mathrm{del}}(\mathbf{I}+\mathbf{L}_{\mathrm{out}})^{-1}\left[\mathbf{L}_{\mathrm{out}}{\mathbf{G}_{\mathrm{cL}}}^{-1}\mathbf{G}_{\mathrm{oL}} - \mathbf{L}_{\mathrm{out}}{\mathbf{G}_{\mathrm{cL}}}^{-1}\mathbf{I}_{\mathrm{L1}}\mathbf{G}_{\mathrm{PLL}} - \mathbf{D}\mathbf{G}_{\mathrm{PLL}}\right] \quad (36)$$

$$\mathbf{G}_{\mathrm{ci}}^{\mathrm{out}} = \mathbf{G}_{\mathrm{ci}}(\mathbf{I}+\mathbf{L}_{\mathrm{out}})^{-1}\mathbf{L}_{\mathrm{out}}{\mathbf{G}_{\mathrm{cL}}}^{-1} \quad (37)$$

$$\mathbf{Y}_{\mathrm{o}}^{\mathrm{out}} = \mathbf{Y}_{\mathrm{o}} + \mathbf{G}_{\mathrm{co}}\mathbf{G}_{\mathrm{del}}(\mathbf{I}+\mathbf{L}_{\mathrm{out}})^{-1}\left[\mathbf{L}_{\mathrm{out}}{\mathbf{G}_{\mathrm{cL}}}^{-1}\mathbf{G}_{\mathrm{oL}} - \mathbf{L}_{\mathrm{out}}{\mathbf{G}_{\mathrm{cL}}}^{-1}\mathbf{I}_{\mathrm{L1}}\mathbf{G}_{\mathrm{PLL}} - \mathbf{D}\mathbf{G}_{\mathrm{PLL}}\right] \quad (38)$$

$$\mathbf{G}_{\mathrm{co}}^{\mathrm{out}} = \mathbf{G}_{\mathrm{co}}(\mathbf{I}+\mathbf{L}_{\mathrm{out}})^{-1}\mathbf{L}_{\mathrm{out}}{\mathbf{G}_{\mathrm{cL}}}^{-1}, \quad (39)$$

where the output-current loop gain $\mathbf{L}_{\mathrm{out}} = \mathbf{G}_{\mathrm{cc}}\mathbf{G}_{\mathrm{del}}\mathbf{G}_{\mathrm{cL}}$.

In Fig. 2, the matrix $\mathbf{G}_{\mathrm{PLL}}$ contains the PLL transfer functions which can be expressed as [17]

$$\mathbf{G}_{\mathrm{PLL}} = \begin{bmatrix} 0 & 0 \\ 0 & G_{\mathrm{PLL}} \end{bmatrix}, \quad (40)$$

$$G_{\mathrm{PLL}} = \frac{1}{U_{\mathrm{od}}}\frac{L_{\mathrm{PLL}}}{1+L_{\mathrm{PLL}}}, \quad (41)$$

$$L_{\mathrm{PLL}} = -G_{\mathrm{PI-PLL}}\frac{U_{\mathrm{od}}}{s}, \quad (42)$$

$$G_{\mathrm{PI-PLL}} = K_{\mathrm{p}} + \frac{K_{\mathrm{i}}}{s}. \quad (43)$$

For the PLL PI-controller, $K_{\mathrm{p}} = 0.67$ and $K_{\mathrm{i}} = 38.02$.

REFERENCES

[1] B. K. Bose, "Energy, environmental pollution, and the impact of power electronics," *IEEE Ind. Electron. Mag.*, pp. 6–17, Mar. 2010.

[2] S. Valkealahti, "Forecasting the future of renewables," in *Climate Change-Socioeconomic Effects*, Sep. 2010, pp. 425–440.

[3] M. Liserre, F. Blaabjerg, and S. Hansen, "Design and control of an LCL-filter-based three-phase active rectifier," *IEEE Trans. Ind. Appl.*, vol. 41, no. 5, pp. 1281–1291, Sep. 2005.

[4] M. Liserre, F. Blaabjerg, and A. DellAquila, "Step-by-step design procedure for a grid-connected three-phase PWM voltage source converter," *Int. J. Electron.*, vol. 91, no. 8, pp. 445–460, 2004.

[5] L. Jessen and F. W. Fuchs, "Modeling of inverter output impedance for stability analysis in combination with measured grid impedances," in *IEEE PEDG'15*, Jun. 2015, pp. 1–7.

[6] N. P. W. Strachan and D. Jovcic, "Stability of a variable-speed permanent magnet wind generator with weak ac grids," *IEEE Transactions on Power Delivery*, vol. 25, no. 4, pp. 2779–2788, Oct 2010.

[7] C. Li, "Unstable operation of photovoltaic inverter from field experiences," *IEEE Trans. Power Del.*, vol. 33, no. 2, pp. 1013–1015, April 2018.

[8] M. Rasheduzzaman, J. A. Mueller, and J. W. Kimball, "An accurate small-signal model of inverter- dominated islanded microgrids using *dq* reference frame," *IEEE Trans. Emerg. Sel. Topics Power Electron.*, vol. 2, no. 4, pp. 1070–1080, Dec. 2014.

[9] A. Aapro, T. Messo, and T. Suntio, "An accurate small-signal model of a three-phase VSI-based photovoltaic inverter with LCL-filter," in *IEEE ICPE- ECCE'15 Asia*, 2015, pp. 2267–2274.

[10] E. Figueres, G. Garcera, J. Sandia, F. Gonzalez-Espin, and J. C. Rubio, "Sensitivity study of the dynamics of three-phase photovoltaic inverters with an lcl grid filter," *IEEE Trans. Ind. Electron.*, vol. 56, no. 3, pp. 706–717, Mar. 2009.

[11] D. Boroyevich and F. Lee, "Novel reduced-order small-signal model of a three-phase PWM rectifier and its application in control design and system analysis," *IEEE Trans. Power Electron.*, vol. 13, no. 3, pp. 511–521, May 1998.

[12] Z. Liu, J. Liu, D. Boroyevich, R. Burgos, and T. Liu, "Small-signal terminal-characteristics modeling of three-phase droop-controlled inverters," in *IEEE ECCE'16*, Sep. 2016, pp. 1–7.

[13] K. M. Alawasa, Y. A. R. I. Mohamed, and W. Xu, "Active mitigation of subsynchronous interactions between pwm voltage-source converters and power networks," *IEEE Trans. Power Electron.*, vol. 29, no. 1, pp. 121–134, Jan. 2014.

[14] M. Cespedes and J. Sun, "Impedance modeling and analysis of grid-connected voltage-source converters," *IEEE Trans. Power Electron.*, vol. 29, no. 3, pp. 1254–1261, Mar. 2014.

[15] J. Sun, "Impedance-based stability criterion for grid-connected inverters," *IEEE Trans. Power Electron.*, vol. 26, no. 11, pp. 3075–3078, Nov. 2011.

[16] J. L. Agorreta, M. Borrega, J. López, and L. Marroyo, "Modeling and control of N-paralleled grid-connected inverters with LCL filter coupled due to grid impedance in pv plants," *IEEE Trans. Power Electron.*, vol. 26, no. 3, pp. 770–785, Mar. 2011.

[17] T. Messo, J. Jokipii, A. Mäkinen, and T. Suntio, "Modeling the grid synchronization induced negative-resistor-like behavior in the output impedance of a three-phase photovoltaic inverter," in *IEEE PEDG'13*, Jul. 2013, pp. 1–7.

[18] J. Puukko and T. Suntio, "Modelling the effect of non-ideal load in three-phase converter dynamics," *Electronics Letters*, vol. 48, no. 7, pp. 402–404, Mar. 2012.

[19] H. Liu, L. Yu, H. Wu, G. Liu, and W. Wang, "Small signal modeling and stability analysis on parallel photovoltaic inverters in microgrid," in *IEEE ECCE'15*, Sep. 2015, pp. 3754–3759.

[20] S. Dutta, D. Debnath, and K. Chatterjee, "A grid-connected single-phase transformerless inverter controlling two solar pv arrays operating under different atmospheric conditions," *IEEE Trans. Ind. Electron.*, vol. 65, no. 1, pp. 374–385, Jan. 2018.

[21] S. Mortazavian and Y. A. R. I. Mohamed, "Dynamic analysis and improved lvrt performance of multiple dg units equipped with grid-support functions under unbalanced faults and weak grid conditions," *IEEE Trans. Power Electron.*, vol. PP, no. 99, pp. 1–1, 2017.

[22] A. Rygg, M. Molinas, C. Zhang, and X. Cai, "On the equivalence and impact on stability of impedance modeling of power electronic converters in different domains," *IEEE Trans. Emerg. Sel. Topics Power Electron.*, vol. 5, no. 4, pp. 1444–1454, Dec. 2017.

[23] L. Nousiainen, J. Puukko, A. Maki, T. Messo, J. Huusari, J. Jokipii, J. Viinamaki, D. T. Lobera, S. Valkealahti, and T. Suntio, "Photovoltaic generator as an input source for power electronic converters," *IEEE Trans. Power Electron.*, vol. 28, no. 6, pp. 3028–3038, Jun. 2013.

[24] R. D. Middlebrook, "Small-signal modeling of pulse-width modulated switched-mode power converters," *Proceedings of the IEEE*, vol. 76, no. 4, pp. 343–354, Apr 1988.

[25] T. Roinila, J. Huusari, and M. Vilkko, "On frequency-response measurements of power-electronic systems applying MIMO identification techniques," *IEEE Trans. Ind. Electron.*, vol. 60, no. 11, pp. 5270–5276, Nov. 2013.